JACS
JOURNAL OF THE AMERICAN CHEMICAL SOCIETY
Article
pubs.acs.org/JACS

Structurally Defined Nanoscale Sheets from Self-Assembly of Collagen-Mimetic Peptides

Tao Jiang,[†] Chunfu Xu,[†] Yang Liu,[†] Zheng Liu,[†] Joseph S. Wall,[‡] Xiaobing Zuo,[§] Tianquan Lian,[†] Khalid Salaita,[†] Chaoying Ni,[¶] Darrin Pochan,[¶] and Vincent P. Conticello*,[†]

[†]Department of Chemistry, Emory University, Atlanta, Georgia 30322

[‡]Brookhaven National Laboratory, Upton, New York 11973

[§]X-ray Science Division, Argonne National Laboratory, 9700 South Cass Avenue, Argonne, Illinois 60439

[¶]Department of Materials Science and Engineering, University of Delaware, Newark, Delaware 19716

Supporting Information

ABSTRACT: We report the design of two collagen-mimetic peptide sequences, **NSI** and **NSII**, that self-assemble into structurally defined nanoscale sheets. The underlying structure of these nanosheets can be understood in terms of the layered packing of collagen triple helices in two dimensions. These nanosheet assemblies represent a novel morphology for collagen-based materials, which, on the basis of their defined structure, may be envisioned as potentially biocompatible platforms for controlled presentation of chemical functionality at the nanoscale. The molecularly programmed self-assembly of peptides **NSI** and **NSII** into nanosheets suggests that sequence-specific macromolecules offer significant promise as design elements for two-dimensional (2D) assemblies. This investigation provides a design rubric for fabrication of structurally defined, peptide-based nanosheets using the principles of solution-based self-assembly facilitated through complementary electrostatic interactions.

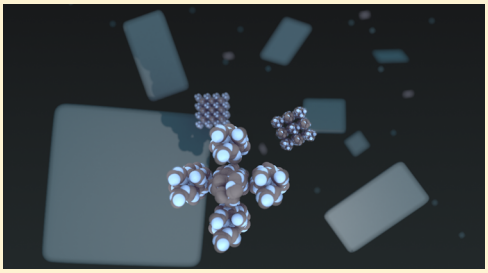

INTRODUCTION

Nanosheets (i.e., two-dimensional (2D) nanoscale assemblies) bridge an important intellectual and physical gap between low-dimensional assemblies (i.e., nanoparticles, nanofibers, nanotubes, and nanoribbons) and extended three-dimensional structures (i.e., crystalline solids). The controlled fabrication of two-dimensional assemblies on the nanoscale presents a significant challenge to current synthetic methods. Nonetheless, the development of effective strategies for the creation of 2D assemblies is essential to the success of the emergent field of 2D nanoarchitectonics,[1,2] in which chemical and physical principles are applied to engineer nanosheet structures for integration into functional devices.

The molecularly programmed self-assembly of sequence-defined peptides offers significant promise for the fabrication of 2D nanoarchitectonics. Peptides have a high density of chemical functionality that can be arranged within a defined macromolecular architecture. This molecular-level information can be utilized within a given structural context to direct highly specific intra- and intermolecular interactions that promote self-assembly of thermodynamically stable and structurally defined 2D assemblies. Despite these advantages, the design of peptide-based two-dimensional assemblies has been limited to structures derived from short linear[3,4] or cyclic peptide sequences,[5] in which the intrinsic conformational properties of the polypeptide backbone have not been utilized as an explicit design principle. However, recent reports from Zuckermann et al.[6] on the controlled fabrication of nanosheets from self-assembly of a sequence-defined peptoid oligomers suggest that this approach has merit, particularly if a stable conformational state of the peptide sequence can geometrically promote specific intermolecular interactions within a two-dimensional assembly.

Collagen-mimetic peptides were selected as a substrate for the design of two-dimensional peptide-based assemblies. Whereas native collagen isoforms display a wide range of morphologies, the formation of 2D assemblies is an uncommon occurrence limited to in vitro conditions.[7] In order to bias self-assembly of collagen-mimetic peptides toward formation of layered collagen structures, methods must be developed to control registry between chains in a triple helix and between adjacent triple helices in supramolecular assemblies. However, despite recent progress, the sequence−structure correlations that determine the differences in structural hierarchy between native collagen isoforms are not well understood at the molecular level.

Previous researchers have demonstrated that introduction of structural modifications into collagen-mimetic peptides can recapitulate the complex modes of native collagen assembly. Metal ion coordination,[8,9] $\pi\pi$ interaction,[10] CH-π interaction,[11] cation-π interaction,[12] and disulfide bond formation[13,14] have been employed to direct higher order assembly of collagen-mimetic peptides into supramolecular structures including fibers, disks, networks, and spherical assemblies. However, the mode of assembly has been difficult to reliably predict from consideration

Received: December 18, 2013
Published: February 26, 2014

dx.doi.org/10.1021/ja412867z | J. Am. Chem. Soc. 2014, 136, 4300−4308

of the initial peptide sequence, such that the resultant assemblies usually do not exhibit the high degree of order implicit within the structural hierarchy of native collagen isoforms.

Previously, we employed sequence-encoded electrostatic interactions to enforce alignment of a designed collagen-mimetic peptide, **CPII**,[15] into uniaxially oriented fibrils (Figure 1). The

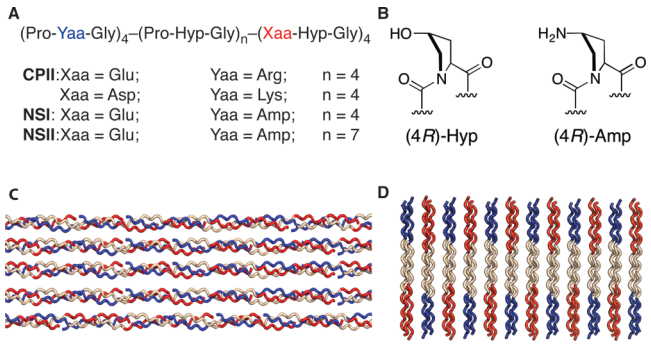

Figure 1. (A) Amino acid sequences of peptides (red: negatively charged amino acids or triads; blue: positively charged amino acids or triads). (B) Structures and preferred ring pucker conformers of imino acid derivatives. (C) Staggered orientation of peptides indicating alignment within synthetic collagen-mimetic fibrils. (D) Proposed packing of collagen triple helices within two-dimensional layers through electrostatic interactions.

design of peptide **CPII** comprised a symmetric sequence of three blocks of four triads, in which the triad sequence within each block encompassed different electrostatic properties. This block architecture was designed to promote a staggered alignment of peptides within a triple helical conformation in order to drive fibrillization through charge complementation (Figure 1C). The **CPII** peptide was observed to self-assemble into fibrils that mimicked the banded, *D*-periodic ultrastructure of native collagen fibers.[16] However, the desired structural alignment was difficult to control under the extensive range of experimental conditions that were investigated for this peptide system. Hartgerink and co-workers, based on an extensive structural analysis of electrostatic interactions within collagen-mimetic peptides,[17] designed a derivative of **CPII** in which conservative substitutions of Asp for Glu and Lys for Arg were incorporated into the peptide sequence (Figure 1A).[18] This second generation peptide underwent multihierarchical self-assembly under a wide range of experimental conditions to afford collagen-based hydrogels composed of laterally associated peptide fibrils.

RESULTS AND DISCUSSION

Although fibrillar morphologies have been the predominant species observed thus far from self-assembly of **CPII**-like peptides, two-dimensional assemblies are not necessarily precluded based on the initial sequence design (Figure 1D). Indeed, the formation of irregular sheet-like structures was occasionally observed from buffered aqueous solutions of **CPII** at near-neutral pH (Figure S7). Two sequence variants of the **CPII** peptide, **NSI** and **NSII**, were designed in order to bias self-assembly toward formation of two-dimensional layered assemblies through incorporation of structural features to promote selective interaction between triple helices.

The sequences of peptides **NSI** and **NSII** were based on the original design of **CPII** in that the pattern of positively and negatively charged amino acid residues was maintained to ensure charge complementarity.[15] However, in order to direct the Coulombic interactions between triple helices, the positively charged arginine residues in the first four triads of **CPII** were replaced with the noncanonical imino acid, (2*S*,4*R*)-4-aminoproline (Amp) (Figure 1B).[19] The stereoelectronic properties of Amp residue mirror those of the canonical (2*S*,4*R*)-4-hydroxyproline (Hyp) residue, in that the pyrrolidine ring adopts a Cγ-*exo* ring pucker conformation.[20] Crystallographic analyses of collagen structures have demonstrated that the Cγ–*exo* ring pucker is the most common conformation for imino acid residues at Yaa positions within the triple helix.[21] The sequence of **NSI** is a direct structural analogue of the parent peptide **CPII**, whereas the sequence of **NSII** differs in that the central block of canonical (Pro-Hyp-Gly) triads was lengthened to seven repeats. Because peptide **NSII** no longer mimics the symmetric triblock architecture of **CPII**, it should not be competent for staggered assembly into one-dimensional fibrils (Figure 1C).

Circular dichroism (CD) spectropolarimetry of solutions of **NSI** (2 mg/mL) and **NSII** (2.5 mg/mL) in MOPS buffer displayed a characteristic collagen triple helical conformation, consisting of a positive maximum at 224 nm and a negative minimum at 198 nm (Figure 2A). The RPN values, that is, the ratio of intensities of the positive CD signal at 224 nm to the negative CD signal at 198 nm,[22] were 0.10 and 0.11 for the solutions of **NSI** and **NSII**, respectively. An RPN value of ≥0.10

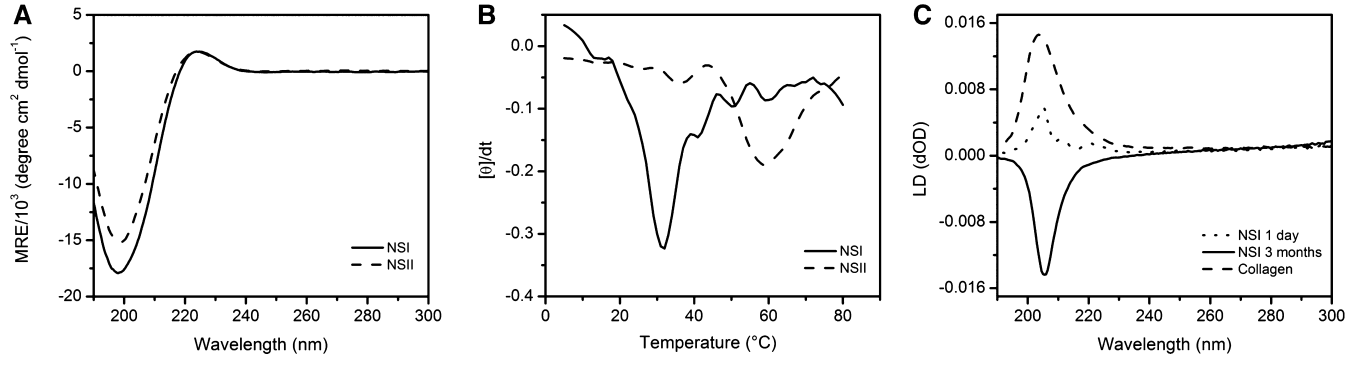

Figure 2. (A) Circular dichroism spectra of peptides **NSI** (2 mg/mL) and **NSII** (2.5 mg/mL) in 20 mM MOPS buffer, pH 7.0. (B) First derivative of the CD signal at 224 nm as a function of temperature. The T_m is estimated from the minimum in the first derivative curve. (C) Flow linear dichroism spectra of nascent (0.5 mg/mL) and assembled (0.5 mg/mL) solutions of **NSI** in 20 mM MOPS buffer, pH 7.0 under a Couette flow of 2000 rpm. The flow LD spectrum of fibrillar type I collagen from rat tail (0.4 mg/mL) in phosphate buffer solution (100 mM, pH 7.4) was employed under identical conditions as a standard of comparison.

dx.doi.org/10.1021/ja412867z | *J. Am. Chem. Soc.* 2014, 136, 4300–4308

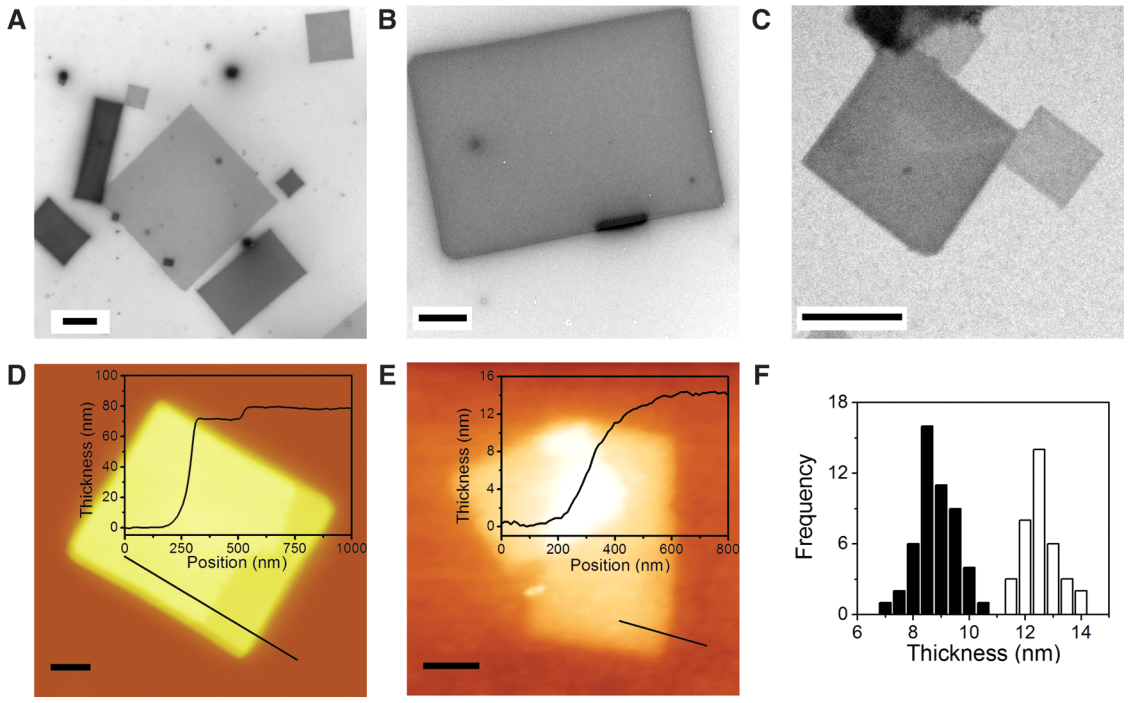

Figure 3. (A) TEM image of **NSI** nanosheets indicating the polydisperse distribution of lateral size and thickness (scale bar = 1 μm). (B) TEM image of an individual **NSI** nanosheet (scale bar = 1 μm). (C) TEM image of representative nanosheets of **NSII** (scale bar = 500 nm). (D) AFM image and height profile (inset) of a multilayer nanosheet of **NSI** (scale bar = 200 nm). (E) Representative AFM image and height profile (inset) of a single-layer nanosheet of **NSII** (scale bar = 200 nm). (F) AFM height histogram for single-layer sheets of **NSI** (black) and **NSII** (white).

is consistent with a stable triple helical structure. Thermal denaturation studies were performed on solutions of the corresponding peptides, which afforded melting transitions (T_m) of 32 and 60 °C for **NSI** and **NSII**, respectively (Figure 2B). The presence of three additional triads of (Pro-Hyp-Gly) in the central block of **NSII** increased the thermal stability of the triple helical conformation vis-à-vis that of **NSI**. The T_m values observed for solutions of **NSI** and **NSII** were significantly below the values expected for collagen-mimetic peptides containing an identical number of canonical (Pro-Hyp-Gly) triads. These data suggest that the aminoproline and glutamic acid residues within the **NSI** and **NSII** peptides thermodynamically destabilize the triple helical conformation. In a previous study, Ganesh et al.[19] have demonstrated that Amp could be substituted in place of hydroxyproline (Hyp) in a collagen peptide consisting of six triad repeats (Pro-Amp-Gly). The corresponding peptide adopted a triple helical structure that was stable at both acidic and basic pH to a greater degree than a peptide of identical length based on the canonical triad repeat sequence (Pro-Hyp-Gly). However, these comparisons were drawn from CD spectropolarimetry of the corresponding peptides that was performed in the presence of 100 mM NaCl, which effectively screened the charge repulsion between Amp residues.

Flow linear dichroism[23] spectra were acquired under shear alignment for solutions of **NSI** as a function of incubation time to interrogate for the formation of assemblies (Figure 2C). The sign and magnitude of the absorbances in flow linear dichroism can be correlated with the direction of polarization of the amide bond chromophores, which can be related to the orientation of self-assembled species in the flow field. Net orientation occurs for anisotropic self-assembled structures that persist under Couette flow. Solutions of freshly dissolved **NSI** displayed a weak positive absorbance at a position coincident with that expected for collagen fibrils.[24] However, incubation of the **NSI** solutions for a period of weeks at 4 °C resulted in a significant change in the flow LD spectrum. The amide bond absorbance displayed a polarization that was opposite to that of the initially prepared **NSI** specimen as well as that of fibrillar Type I collagen. The intensity of the signal for the mature **NSI** assemblies also increased significantly in comparison to the initial sample, approaching that of the fibrillar collagen preparation. The flow LD data support the formation of extended assemblies of **NSI**, in which the collagen triple helices are oriented in the flow field such that the long axis of the triple helix is perpendicular to the direction of flow. This arrangement would be consistent with assemblies consisting of layers of perpendicularly oriented collagen triple helices (Figure 1D). Surprisingly, a corresponding flow LD signal was not observed for assemblies derived from the more thermodynamically stable **NSII**. Subsequent studies indicated that the **NSII** assemblies were less robust toward shear alignment, which resulted in dis-assembly of the supramolecular structures under Couette flow (vide infra).

The flow LD data suggested that solutions of **NSI** and, by association, **NSII**, could self-assemble into supramolecular structures in solution. The formation of the assemblies was confirmed through correlative analysis with transmission electron microscopy (TEM) and atomic force microcopy (AFM) (Figure 3). The self-assembly of **NSI** and **NSII** peptides in solution was monitored over time. The rate of formation of the assemblies was observed to depend on the concentration and molar mass of the peptide and ranged from weeks to hours. Dilute solutions of **NSI** (2 mg/mL in 20 mM MOPS, pH 7.0) assembled over a period of weeks, although more concentrated solutions (4 mg/mL) formed assemblies over a period of days. In contrast, solutions of **NSII** (2.5 mg/mL in 20 mM MOPS, pH 7.0) assembled over a period of hours. Analytical HPLC of **NSI** (2 mg/mL) and **NSII** (2.5 mg/mL) solutions indicated that approximately 46% and 30% of the respective peptides remained

dx.doi.org/10.1021/ja412867z | J. Am. Chem. Soc. 2014, 136, 4300−4308

in solution after centrifugation (Supporting Figures S8 and S9). These results suggest that a significant fraction of either peptide sediments as self-assembled species.

TEM analysis of **NSI** and **NSII** assemblies was consistent with the presence of two-dimensional nanoscale sheets as the only observable self-assembled structures (Figure 3A–C). Most commonly, the sheets occurred as fully formed tetragonal assemblies with cleanly defined edges in both lateral dimensions. On occasion, sheets were observed in stages of incomplete growth, in which well-defined terraces could be detected (Figure S10). Typically, the nanosheets displayed a wide dispersion in lateral dimensions; this polymorphism may be attributable to slow nucleation kinetics for sheet formation. This effect was more pronounced for sheets derived from **NSI** in comparison to **NSII**. In the former case, polymorphism could be detected not only in the plane of the sheet but also in the direction normal to the plane. In the TEM images of **NSI** sheets, this dispersion in height was manifested in terms of differences in the electron contrast among the assemblies (Figure 3A). An equimolar mixture of the two peptides, **NSI** and **NSII**, did not appear to form mixed species but rather a mixed population of nanosheets that were characteristic of the individual peptides (Supporting Figure S11).

AFM analysis was employed to interrogate the height of the assemblies, which was observed to depend on the concentration and molar mass of the peptides (Figure 3D–F). Solutions of **NSI** incubated for long periods under dilute conditions (2 mg/mL) afforded much thicker nanosheets, with heights up to ca. 250 nm. More concentrated solutions of **NSI** (4 mg/mL) and solutions of **NSII** (2.5 mg/mL) afforded thinner sheets. Nanosheets of **NSII** were typically only one or two layers in thickness (Figure 3E). This observation may explain the absence of a flow LD signal for **NSII**, as these thinner sheets are not significantly robust to withstand the shear forces necessary for alignment. TEM analysis of shear-aligned samples of **NSII** nanosheets indicated significant fragmentation subsequent to attempted alignment within a Couette cell. For the thicker sheets of **NSI**, AFM provided evidence for multiple stacked layers of collagen peptides, as terraces could be observed on the surface of the sheets that corresponded to growth of new layers (Figure 3D). AFM measurements provided values of 8.8 ± 0.8 nm and 12.3 ± 0.7 nm for the heights of single-layer sheets of **NSI** and **NSII**, respectively (Figure 3F). The calculated thickness for a layer comprising vertically oriented triple helices of **NSI** and **NSII** should be 10.3 and 12.9 nm, respectively (no. of residues × 0.286 nm rise/residue).[25] These data suggest that the nanosheets are composed of stacked layers of collagen triple helices. The difference in layer height between nanosheets derived from **NSI** and **NSII** could be attributed to the respective differences in peptide length projected onto a collagen triple helix.

The well-defined morphology of the **NSI** and **NSII** nanosheets suggested an ordered internal structure. The thicker assemblies derived from peptide **NSI** proved more physically robust to structural analysis and were studied in further detail. Synchrotron SAXS/WAXS data were collected on aqueous solutions of **NSI** in MOPS buffer. The resultant plot of intensity versus momentum transfer (q) displayed a complex dependence in which form factor scattering was convoluted with sharp Bragg reflections (Figure 4A). The scattering intensity in the Porod region followed a power law dependence of the momentum transfer (q^{-2}).[26] The mass fractal dimension confirmed the sheet-like structure in solution (Figure S12). However, the dispersion in

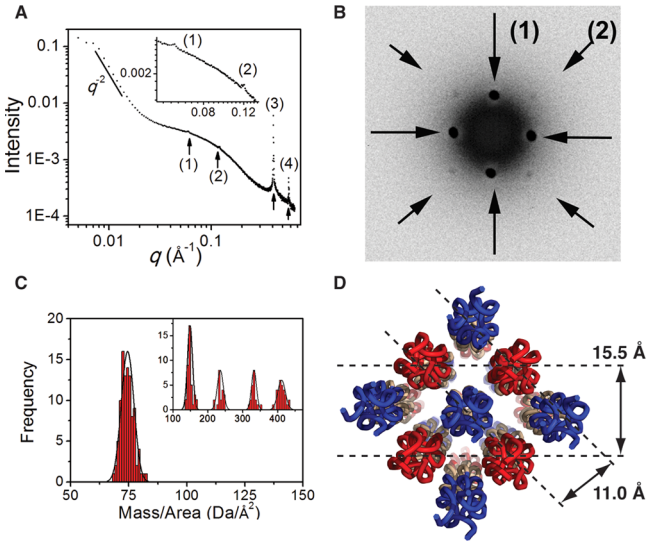

Figure 4. (A) Synchrotron SAXS scattering profile for solutions of **NSI** sheets showing q^{-2} dependence in the Porod region and diffraction peaks. Peaks (d-spacing): (1), 105 Å; (2), 52.4 Å; (3), 15.5 Å; and (4), 11.0 Å. Inset: expansion of the scattering profile corresponding to peaks (1) and (2). (B) Electron diffraction pattern from **NSI** sheets. Diffraction spots were observed at 15.2 Å (1) and 10.8 Å (2) (C) Mass per area measurements for **NSI** nanosheets in the single-layer and multilayer (inset) regions. (D) Structural model of the 2D lattice of **NSI** sheets in a tetragonal arrangement of antiparallel triple helices.

sheet thickness prevented extraction of the single-layer sheet height using Guinier analysis.

In the higher q region, four diffractions signals were observed—two peaks of relatively weak intensity at q values of 0.0600 and 0.120 Å^{-1} and two strong, sharp peaks at q values of 0.405 and 0.573 Å^{-1}. The former signals correspond to d-spacings of 105 Å and 52.4 Å. The larger distance of 10.5 nm was consistent with the height of a single layer of laterally aligned collagen triple helices derived from **NSI** (vide supra). The smaller spacing of 52.4 Å was approximately half that of the 105 Å spacing, which suggested that the larger distance corresponds to that of a (001) lattice plane while the smaller one is consistent with the (002) plane. The observation of a diffraction peak associated with the (002) plane suggests that the triple helices within a layer may be packed with an antiparallel orientation between nearest neighbors (vide infra). The weak intensity of these two reflections is indicative of the limited layer stacking in the z-direction (i.e., perpendicular to the surface of the two-dimensional sheet).

The more intense signals at larger q values correspond to d-spacings of 15.5 and 11.0 Å, which fall into the regime of reported intertriple helical distances from crystal structures of collagen-mimetic model peptides.[21,27−31] Interestingly, these two d-spacings are related in that the 15.5 Å distance is equal to $\sqrt{2}$ times the 11.0 Å distance, which suggests that a two-dimensional tetragonal lattice may underlie the layered packing of collagen triple helices in nanosheets of **NSI**. The crystal structures of collagen-mimetic peptide sequences can be sorted into two symmetry classes based on pseudohexagonal and pseudotetragonal packing of triple helices, respectively. The packing of the 2D lattice of the **NSI** nanosheets more closely approximates the packing of the latter structures, although the dimensions of the lattice are contracted from the lattice parameters typically observed for pseudotetragonal packing within the crystal

dx.doi.org/10.1021/ja412867z | J. Am. Chem. Soc. 2014, 136, 4300−4308

structures of collagen-mimetic peptides (e.g., PDB IDs: 1 ITT, 1X1K, 2 CUO, 2D3F, 2D3H, 3ADM, 3AH9, 3A1H, and 3AI6).[21,31]

Electron diffraction (ED) data (Figure 4B) from nanosheets of **NSI** provide additional support for a 2D lattice of perpendicularly oriented collagen triple helices. Sharp diffraction spots are observed at *d*-spacings of 15.2 and 10.8 Å, which are nearly identical to those observed in the solution SAXS measurements. A 4-fold rotational symmetry was observed for the major and minor diffraction lattices, with a 45° angular offset between the two lattices. Lattice orientations for the larger *d*-spacing coincided with the directions of the sheet edges in the corresponding TEM image (Figure S13). The symmetry and lattice spacings of the **NSI** nanosheets were compared to the pseudotetragonal packing of triple helices in the *ab*-plane from the crystal structure of a representative collagen-mimetic model peptide (PDB ID: 3AI6). The comparative data suggest that the 2D lattice of the **NSI** nanosheets comprises a unit cell of 22 Å × 22 Å containing four triple helices. The 15.5 and 11.0 Å *d*-spacings correspond to reflections from the (110) and (200)/(020) lattice planes, respectively (Figure 4D). Diffraction peaks of similar intensity can be calculated for the corresponding lattice planes in the crystal structure of the collagen-mimetic peptide (Figure S14 and Table S1).[21,31]

In addition, scanning transmission electron microscopy (STEM)[32] was employed to measure the mass-per-area (M/A)[3,33] of freeze-dried specimens of **NSI** nanosheets. Single-layer sheets of **NSI** were observed to have an average mass-per-area value of 75 Da/Å^2 (Figures 4C and S15). A theoretical mass-per-area of 83 Da/Å^2 was calculated for a 22 Å × 22 Å tetragonal unit cell containing four triples helices with individual masses of 10 044 Da derived from trimers of the **NSI** peptide (Figure 4D). The calculated and experimentally determined M/A values compare well within the error limits of the STEM analysis. Moreover, multilayer sheets of **NSI** displayed a progression of M/A values between layers that differed by increments of approximately 80 Da/Å^2 (Figure 4C, inset, and Figure S16). This observation further substantiated a packing arrangement in which collagen layers were successively laminated to form the thick nanosheets derived from self-assembly of **NSI**.

The well-ordered peptide packing within the nanosheets suggests that the surfaces of the assemblies should be decorated with functional groups derived from the termini of the peptide (Figure 4D). The functional groups at the sheet surface should be accessible for interaction with exogenous substrates. As a test of this hypothesis, nanosheets derived from **NSII** were probed with cationic gold nanoparticles (10 nm core diameter functionalized with (11-mercaptoundecyl)-*N*,*N*,*N*-trimethylammonium bromide). The **NSII** sheets were chosen as substrates based on their greater thermodynamic stability due to the increased peptide length vis-à-vis sheets derived from **NSI**. The positively charged ammonium ions immobilized on the gold nanoparticles should interact selectively with the negatively charged *C*-terminal carboxylate groups of the peptides. TEM and AFM analysis provide evidence for relatively dense packing of the nanoparticles at the surface of **NSII** nanosheets (Figure 5 A,B). The diameter of the nanoparticles is much larger than the distance between adjacent triple helices in the structure (ca. 11−15 Å). The nanoparticles tend to spread out evenly on the surface at lateral spacings that are larger than the nanoparticle diameter. Fourier transforms of the TEM images do not provide evidence for an ordered arrangement of nanoparticles on the surface, which may indicate either that the system has not achieved equilibrium

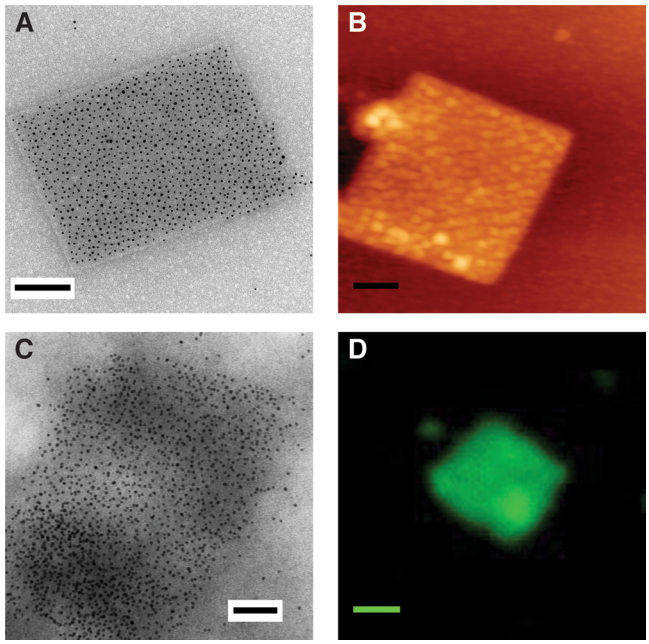

Figure 5. (A) TEM image of **NSII** nanosheet probed with cationic gold nanoparticles (scale bar = 200 nm). (B) AFM image of **NSII** nanosheet probed with cationic gold nanoparticles (scale bar = 400 nm). (C) TEM of **NSII*** nanosheets probed with streptavidin-tagged gold nanoparticles (scale bar = 100 nm). (D) Fluorescence microscopy image of **NSII*** nanosheets immobilized on a biotinylated glass surface and stained with streptavidin-Alexa488 (scale bar = 2 μm).

under the experimental conditions or that the surface functional groups may adopt a more disordered arrangement than the internal structure of the assembly.

In order to promote a more specific interaction between the gold nanoparticles and nanosheets, a variant of peptide **NSII**, **NSII***, was synthesized in which the *N*-terminus was capped with the *D*-biotin-15-amido-4,7,10,13-tetraoxapentadecyl group (biotin-dPEG$_4$). CD spectropolarimetry of peptide **NSII*** (2.8 mg/mL) in MOPS buffer (20 mM, pH 7.0) indicates the presence of the triple helical conformation of collagen, although the RPN value of 0.083 and T_m value of 54 °C suggest that the structure is less stable than that of **NSII** (Figures S18 and S19). **NSII*** self-assembles into nanosheets of similar morphology to **NSII** assemblies under identical conditions (Figure S20). Nanosheets derived from **NSII*** bind selectively to streptavidin-tagged gold nanoparticles (10 nm core diameter) with high affinity (Figure 5C). In contrast, nanosheets of **NSII** show no tendency to bind streptavidin-tagged gold nanoparticles (Figure S21). The nanoparticle binding appears more dense and less uniform than the corresponding interaction of the **NSII** nanosheets with cationic gold nanoparticles (Figure 5A,B). The strength of the biotin−streptavidin interaction dictates that the binding of the nanoparticles is kinetically irreversible in the former case, which explains the differences in particle distribution at the sheet surface.

The biotin−streptavidin interaction could also be employed to selectively immobilize nanosheets of **NSII*** on functionalized surfaces (Figures 5D and S22). Biotin-derivatized glass surfaces were treated with excess streptavidin, followed by incubation with preassembled nanosheets of **NSII***. The immobilized nanosheets were visualized using fluorescence microscopy after treatment with a solution of streptavidin-tagged Alexa488 dye. Reflection interference contrast microscopic (RICM) indicated

dx.doi.org/10.1021/ja412867z | *J. Am. Chem. Soc.* 2014, 136, 4300−4308

that the fluorescent signal colocalized with the nanosheet (Figure S22). In general, the biotin-capped nanosheets of **NSII*** could be immobilized on the surface with retention of the 2D shape. However, structural remodeling was also noted for some nanosheets upon immobilization, perhaps due to the strength of the biotin−streptavidin interaction. Although the **NSII*** nanosheets attached with random orientations to the functionalized surface, these data demonstrate the potential for construction of hybrid nanostructures through programmable noncovalent interactions, which is an essential condition for articulation of the nanosheets into functionally complex 2D nanoarchitectonic platforms.

■ CONCLUSION

Significant research effort over the past two decades has been directed toward creation of structurally complex materials through solution-based self-assembly. However, most studies have focused on the design and fabrication of one-dimensional assemblies (e.g., nanofibrils, nanoribbons, and nanotubes), whereas far fewer examples of structurally defined two-dimensional assemblies have been reported. Sequence-specific macromolecules (i.e., peptides and nucleic acids) represent attractive scaffolds for the creation of these assemblies, in that supramolecular structure can be encoded at the molecular level through the progression of structural hierarchy. DNA nanotechnology has enabled the creation of a diverse range of structurally defined 1D, 2D, and 3D assemblies from simplified molecular building blocks.[34−38] DNA has an advantage in that the Watson−Crick base pairing rules provide a simple scoring function that can be employed to distinguish among alternative structural alignments between protomers in multiple dimensions. In contrast, the rules that govern protein−protein interactions are more complex and difficult to reliably predict. However, the sequence specificity and chemical diversity of peptide-based materials affords the opportunity to introduce functional complexity across length-scales, if the intermolecular structural interactions between subunits could be predicted and controlled.[39] In addition, peptides have the advantage of greater chemical stability and physical robustness in comparison to nucleic acids, as well as being more amenable to preparative-scale synthesis.

Two-dimensional protein-based assemblies have been observed in native biological systems, most notably, the crystalline S-layers associated with bacterial surfaces.[40] Significant research effort has been directed toward modification of the S-layer systems for use in non-native applications as stable two-dimensional platforms for nanotechnology.[41] However, rather than reverse-engineering native protein-based 2D-assemblies, such as S-layers, we have explored an alternative approach in which synthetic peptide sequences were forward engineered to self-assemble into structurally defined two-dimensional assemblies. This approach has scientific precedent in that peptide[3,42] and peptoid[6] oligomers have been synthesized that self-assemble into 2D nanomaterials. The fibrillogenic peptide **CPII** was redesigned to introduce charge complementarity between triple helices in order to promote lateral assembly into layered structures. Biophysical measurements were conducted in solution and the solid-state on assemblies derived from the resultant peptides, **NSI** and **NSII**, over multiple length-scales of structural hierarchy. The accumulated data suggest that the underlying structure of these nanosheets can be understood in terms of the layered packing of collagen triple helices. Moreover, the chemical functionality displayed at the surface of the nanosheet enabled further elaboration of these structures through surface-localized chemical interactions.

Recently, several collagen-mimetic peptides have been reported that self-assemble into supramolecular structures based on 2D lattices.[8e,43] The cohesive interactions between protomers were derived from either metal-promoted cross-linking or heterochiral peptide recognition. However, the **NSI** and **NSII** nanosheets display a very high degree of internal order over large 2D length scales without recourse to introduction of non-native structural interactions. Moreover, the nanosheet thickness can be controlled through the peptide length and terminal functionality. The presence of functionalized capping groups provides the opportunity to control the surface chemistry to promote specific interaction with exogenous substrates that have been complementarily functionalized. Previous investigators have demonstrated that charge complementation is a powerful experimental strategy to control supramolecular structure within peptide-based materials,[6,15,18,44−47] especially when applied in the context of a defined backbone conformation. Our experimental results demonstrate that the collagen triple helix represents a flexible experimental platform for creation of extended self-assembled 2D structures through structurally informed encoding of electrostatic interactions.

■ METHODS

Materials. Chemical reagents were purchased from Sigma-Aldrich Chemical Co. (St. Louis, MO) or Anaspec, Inc. (Fremont, CA), unless otherwise noted. (2*S*, 4*R*)-Boc-4-amino-1-Fmoc-pyrrolidine-2-carboxylic acid (Amp) was purchased from RSP Amino Acids LLC (Shirley, MA). Biotin-dPEG$_4$ acid was purchased from Quanta BioDesign, Ltd. (Powell, OH). Fmoc-Gly-PEG-PS resin for solid-phase synthesis was purchased from Applied Biosystems, Inc. (Foster City, CA). Alexa 488 NHS ester was purchased from Life Technologies, Co. (Carlsbad, CA). Streptavidin was purchased from Rockland Immunochemicals, Inc. (Gilbertsville, PA). Cationic gold nanoparticles (10 nm diameter, functionalized with 11-mercaptoundecyl-*N*,*N*,*N*-trimethylammonium bromide were purchased from Cytodiagnostics, Inc. (Burlington, ON, Canada). Mica surfaces modified with (3-aminopropyl)-triethoxysilane (APTES) were obtained from Novascan Technologies, Inc. (Ames, IA).

Peptide Synthesis. Peptides **NSI** and **NSII** were prepared as the uncapped derivatives using microwave-assisted synthesis on a CEM Liberty solid-phase peptide synthesis instrument using an Fmoc-Gly-PEG-PS resin. Standard Fmoc protection chemistry was employed with coupling cycles based on HBTU/DIEA-mediated activation protocols and base-induced deprotection (20% piperidine in DMF with 0.1 M HOBt) of the Fmoc group. Peptides were purified via RP-HPLC on a C18 column with a gradient of water−acetonitrile with 0.1% trifluoroacetic acid. The target fractions were collected and lyophilized. The mass and purity were analyzed by matrix-assisted laser desorption/ionization (MALDI) mass spectrometry and analytical HPLC (see Supporting Information). Peptides were dialyzed against deionized water thoroughly to remove residual trifluoroacetate (MWCO = 2000 Da). The resulting peptides were relyophilized and stored at −20 °C before use. Peptide **NSII*** was synthesized and purified using an identical procedure, with the exception that the *N*-terminus was capped with biotin-dPEG$_4$, using in situ activation of the corresponding free acid. The presence of the biotin-dPEG$_4$ capping group was confirmed using mass spectrometric analysis (see Supporting Information). Peptides

dx.doi.org/10.1021/ja412867z | *J. Am. Chem. Soc.* 2014, 136, 4300−4308

were dissolved in MOPS buffer (20 mM, pH 7.0) at the desired concentration. Solution concentrations were determined from the measured mass of the respective peptides. Samples were thermally annealed at 75 °C for 45 min and gradually cooled to ambient temperature. For analysis of the relative concentration of free peptide, samples of assembled and unassembled peptides were centrifuged at 16 000*g* for 10 min. The supernatant of the solutions was analyzed using reverse-phase analytical HPLC after addition of trifluoroacetic acid to 0.1% (v/v). The chromatographic traces acquired before and after self-assembly were integrated to calculate the percentage of peptide remaining in solution.

Circular Dichroism Spectropolarimetry. CD spectra were recorded on a Jasco J-810 CD spectropolarimeter in 0.10 mm quartz cells in MOPS buffer (20 mM, pH 7.0). Spectra were recorded from 300 to 190 nm at a scanning rate of 100 nm/min and a resolution of 0.5 nm. CD melting experiments were performed in the temperature range from 5 to 80 °C at a heating rate of 1 °C/min. The intensity of the CD signal at 224 nm was monitored as a function of temperature. Melting temperatures were obtained from the first derivative of the melting curves.

Flow Linear Dichroism Spectroscopy. Flow linear dichroism spectra were recorded on a JASCO J-810 circular dichroism spectropolarimeter using a microvolume cuvette with a path length of 50 μm and a rotation speed of 2000 rpm to establish Couette flow.[48] The background scattering for each sample was obtained from the LD spectra of samples at 0 rpm. The LD spectra were measured after 5 min of rotation. Solutions of **NSI** were sampled in MOPS buffer (20 mM, pH 7.0) at the indicated concentrations (Figure 2C). Type I collagen from rat tail (Sigma-Aldrich Chemical Co.) was prepared in phosphate buffer (100 mM, pH 7.4) at a concentration of (0.4 mg/mL).

Transmission Electron Microscopy. TEM specimens were prepared from aqueous solutions of **NSI** (2 mg/mL), **NSII** (2.5 mg/mL), or **NSII*** (10 mg/mL) in MOPS buffer (20 mM, pH 7.0). The samples were deposited onto 200 mesh carbon-coated copper grids from Electron Microscopy Sciences (Hatfield, PA). After a 2 min incubation period, excess liquid was wicked away, and the specimens were stained with an aqueous solution of uranyl acetate (1%). Excess stain was wicked away after incubation on the grid for 30 s. The sample grids were dried under vacuum and stored in a desiccator. TEM measurements were acquired on a Hitachi H-7500 transmission electron microscope at an accelerating voltage of 75 kV.

For cationic gold nanoparticle staining experiments, both the solution of nanoparticles and **NSII** sheets were diluted 20 times with distilled, deionized H_2O. An aliquot (4 μL) of the diluted cationic gold solution was added to a solution (4 μL) of the diluted **NSII** sheets in situ. The mixture was incubated at ambient temperature for 20 min. Excess liquid was wicked away, and the specimens were then stained with uranyl acetate (1%) for 30 s. Excess stain solution was wicked away. Sample grids were dried in vacuum desiccator before TEM investigation. TEM images were recorded as described above.

Streptavidin-tagged gold nanoparticles were diluted 10−20 times with MOPS buffer (20 mM, pH 7.0). An aliquot (4−20 μL) of the diluted streptavidin-gold solution was added to 4 μL of **NSII*** sheets (10 mg/mL) in situ and was incubated at ambient temperature for 20 min. Excess liquid was wicked away, and the sample was washed three times for 5 min to remove the nonspecifically bound streptavidin−gold solution. The specimens were then stained with uranyl acetate (1%) for 30 s. Excess stain solution was wicked away. Sample grids were dried in vacuum desiccator before TEM investigation. TEM images were recorded as described above.

Electron Diffraction. Electron diffraction patterns were acquired on either a Hitachi H-7500 transmission electron microscope (Emory University) or an FEI Tecnai G^2 12 transmission electron microscope (University of Delaware). Data were acquired from individual **NSI** nanosheets prepared as described above for TEM diffraction pattern acquisition. Adequate camera lengths (1 m for H-7500 and 2.1 m for Tecnai G^2 12) were used to expose the small reciprocal lattice, and *d*-spacings were calculated using the equation: $d = \lambda L/R$, where R is the distance of the diffraction spots, λ denotes the electron wavelength, and L is the camera length. An aluminum polycrystalline standard from Ted Pella, Inc. (Redding, CA) was used to calibrate the camera length.

Atomic Force Microscopy. AFM measurements were performed using either a JEOL JSPM-4200 or MFP-3D-BIO AFM instruments. Aqueous solutions of **NSI** (2 mg/mL) or **NSII** (2.5 mg/mL) in MOPS buffer (20 mM, pH 7.0) were deposited on either a freshly cleaved mica substrate or a precleaned glass coverslip. Silicon AFM tips (MikronMasch) with a force constant (5.4−16 N/m) were used to image the specimens in tapping mode at a scan rate of 1 Hz. A TGZ-20 SiO_2 grating was employed for *z*-axis calibration (Ted Pella). For gold nanoparticle binding experiments, a solution of **NSII** nanosheets was deposited on an APTES-modified mica substrate and was treated with a diluted solution of cationic gold nanoparticles.

Scanning Transmission Electron Microscopy. The STEM data were acquired at Brookhaven National Laboratory (BNL). The STEM instrument operates at 40 keV with a scanning probe of <0.3 nm diameter produced from a cold field-emission source. Every electron emerging from the specimen is detected by one of the scintillator-photomultiplier detectors collecting 0−15 mRadian (bright field), 15−40 mRadian (small-angle dark field), and 40−200 mRadian (large-angle dark field). The large-angle signal is proportional to the mass of atoms in the path of the beam. Specimen quality and mass calibration are checked by detailed comparison of the image to the known structure of tobacco mosaic virus (TMV). For mass-per-area (M/A) measurements, TMV rafts at a theoretical M/A value of 81.9 Da/Å^2 were employed for calibration.

Specimens are deposited on thin carbon (ca. 2 nm thick) supported on a thicker holey carbon film mounted on a titanium grid using the wet-film, hanging-drop method http://www.bnl.gov/biology/stem/SpecPrepDetails.asp. TMV is added to the grid first as an internal control, followed by injection buffer, then specimen solution (in 20 mM MOPS buffer, pH 7.0) for 1 min, then 10 washes of 20 mM ammonium acetate, pH 7.0. Excess solution is wicked from the edge with filter paper between each injection. After the last wash, the grid is wicked to a thin layer (ca. 1 μm), fast frozen by plunging into liquid nitrogen slush, and stored under liquid nitrogen. Grids are freeze dried overnight in an ion-pumped chamber with an efficient cold trap and transferred under vacuum to the STEM cold stage (−160 °C). Imaging typically uses a dose of 20 el/Å^2 (causing <5% mass loss, corrected by comparison to TMV).

Mass measurements were performed off-line with customized software (PCMass, available at ftp.stem.bnl.gov). The program masks out objects significantly above background and computes the value for the thin carbon in the remaining areas, which is subtracted, and pixels within the contour of filaments are summed and divided by area to give mass-per-unit-area. Accuracy is determined by cleanliness of the background between objects

and by counting statistics of the scattered electrons. For TMV, the program provides automatic searching and measurement, but manual selection was employed for the thin sheets. PCMass also provides statistics in a database for individual images or groups of images.

Small- and Wide-Angle X-ray Scattering Measurements. Synchrotron SAXS/WAXS measurements were performed at the 12-ID-B beamline of Advanced Photon Source at Argonne National Laboratory. A simultaneous SAXS/WAXS setup was utilized, and the sample-to-detector distances were set such that the overall scattering momentum transfer, q, range was achieved from 0.005 to 2.4 Å^{-1}, where $q = 4\pi\sin\theta/\lambda$, 2θ denoting the scattering angle and λ the X-ray wavelength. The wavelength was set at 1.033 Å during the measurements. Scattered X-ray intensities were measured using a Pilatus 2 M (DECTRIS Ltd.) detector for SAXS and Pilatus 300K for WAXS. SAXS/WAXS measurements were performed on aqueous solutions of peptide **NSI** at a concentration of 4 mg/mL in MOPS buffer (20 mM, pH 7.0) at 25 °C. A quartz capillary flow cell (1.5 mm diameter) was employed to prevent radiation damage. Twenty images were collected for each sample and buffer. The 2D scattering images were converted to 1D SAXS curves through azimuthal averaging after solid angle correction and then normalizing with the intensity of the transmitted X-ray beam, using the software package at beamline 12ID-B. The 1D curves of the samples were averaged and subtracted with the background measured from the corresponding buffers.

Fluorescence Microscopy. An aliquot (100 μL) of a 1.5 mM solution of Alexa 488 dye was reacted with streptavidin (0.5 mg/mL) in 0.1 M sodium bicarbonate for 1 h. The unreacted Alexa 488 dye was removed with phosphate buffered saline (PBS, pH 7.4) in a *P*-6 gel spin column (Biorad) that was pre-equilibrated with PBS buffer. Silicon glass was etched by piranha solution (v/v = 3:7 hydrogen peroxide/sulfuric acid) for 15 min to remove residual organic materials and then functionalized with 2% (3-aminopropyl) trimethoxysilane in acetone for 4 h. An aliquot (200 μL) of biotin−NHS ester (2 mg/mL) in dimethylsulfoxide was added to the amine-modified surface and was incubated for 3 h. After thoroughly rinsing the surface with deionized water and acetone, an aliquot (500 μL) of streptavidin (50 μg/mL) in PBS solution was incubated with the biotinylated surface for 1 h. The surface was treated with PBS and MOPS buffers (20 mM, pH 7.0) to remove the unbound streptavidin and incubated subsequently with a solution (0.5 mg/mL) of the **NSII*** nanosheets in MOPS buffer (20 mM, pH 7.0) for 1 h. A solution (0.5 mL) of Alexa 488-labeled streptavidin (250 nM) was added to the nanosheet-bound surface for 1 h and subsequently rinsed three times with MOPS buffer (20 mM, pH 7.0).

Conventional fluorescence microscopy was performed using a Nikon Eclipse Ti inverted fluorescence microscope equipped with a Nikon 100X oil-immersion objective (numerical aperture (NA) of 1.49) and an electron multiplying charge-coupled device (Photometrics Evolve or Andor iXon). To image the Alexa 488−streptavidin nanosheets, a Nikon mercury lamp was used as excitation source and a FITC cube (λ_{ex} = 480/40 nm; λ_{em} = 535/50 nm) was employed for wavelength selection. In addition, reflection interference contrast microscopy (RICM) was performed on the same instrument to visualize the contact areas of nanosheets on glass surface. The images were acquired with the Evolve EMCCD feature (106.7 nm/pixel) and Andor iXon feature (60 nm/pixel).

■ ASSOCIATED CONTENT

Supporting Information

Additional experimental characterization of peptides and peptide assemblies. This material is available free of charge via the Internet at http://pubs.acs.org.

■ AUTHOR INFORMATION

Corresponding Author

E-mail: vcontic@emory.edu.

Notes

The authors declare no competing financial interest.

■ ACKNOWLEDGMENTS

V.P.C. acknowledges financial support from NSF grant CHE-1012620. The authors acknowledge Professor Barbara Brodsky for helpful discussions and Dr. I-Lin Wu for acquisition of the mass spectrometric data. We thank Dr. John Bacsa for assistance in the analysis of the crystallographic data from pseudotetragonal collagen structures. This work benefited from the use of the A.P.S. funded by U.S. D.O.E. Office of Basic Energy Sciences, Division of Material Sciences, under contract W-31-109-Eng-38.

■ REFERENCES

(1) Govindaraju, T.; Avinash, M. B. *Nanoscale* **2012**, *4*, 6102−6117.
(2) Ariga, K.; Ji, Q.; Hill, J. P.; Bando, Y.; Aono, M. *NPG Asia Mater.* **2012**, *4*, e17.
(3) Hamley, I. W.; Dehsorkhi, A.; Castelletto, V. *Chem. Commun.* **2013**, *49*, 1850−1852.
(4) Hughes, M.; Xu, H.; Frederix, P. W. J. M.; Smith, A. M.; Hunt, N. T.; Tuttle, T.; Kinloch, I. A.; Ulijn, R. V. *Soft Matter* **2011**, *7*, 10032−10038.
(5) Govindaraju, T.; Pandeeswar, M.; Jayaramulu, K.; Jaipuria, G.; Atreya, H. S. *Supramol. Chem.* **2011**, *23*, 487−492.
(6) (a) Nam, K. T.; Shelby, S. A.; Choi, P. H.; Marciel, A. B.; Chen, R.; Tan, L.; Chu, T. K.; Mesch, R. A.; Lee, B. C.; Connolly, M. D.; Kisielowski, C.; Zuckermann, R. N. *Nat. Mater.* **2010**, *9*, 454−460. (b) Kudirka, R.; Tran, H.; Sanii, B.; Nam, K. T.; Choi, P. H.; Venkateswaran, N.; Chen, R.; Whitelam, S.; Zuckermann, R. N. *Biopolymers* **2011**, *96*, 586−595.
(7) (a) Paige, M. F.; Goh, M. C. *Micron* **2001**, *32*, 355−361. (b) Fujita, Y.; Kobayashi, K.; Hoshino, T. *J. Electron Microsc.* **1997**, *46*, 321−326. (c) Kobayashi, K.; Hashimoto, Y.; Hayakawa, T.; Hoshino, T. *J. Ultrastruct. Mol. Struct. Res.* **1988**, *100*, 255−262. (d) Olsen, B. R. *J. Ultrastruct. Res.* **1967**, *19*, 446−473. (e) Olsen, B. R. *J. Ultrastruct. Res.* **1967**, *19*, 432−445.
(8) (a) Przybyla, D. E.; Chmielewski, J. *J. Am. Chem. Soc.* **2008**, *130*, 12610−12611. (b) Pires, M. M.; Chmielewski, J. *J. Am. Chem. Soc.* **2009**, *131*, 2706−2712. (c) Pires, M. M.; Przybyla, D. E.; Rubert Pérez, C. M.; Chmielewski, J. *J. Am. Chem. Soc.* **2011**, *133*, 14469−14471. (d) Pires, M. M.; Lee, J.; Ernenwein, D.; Chmielewski, J. *Langmuir* **2012**, *28*, 1993−1997. (e) Przybyla, D. E.; Rubert Pérez, C. M.; Gleaton, J.; Nandwana, V.; Chmielewski, J. *J. Am. Chem. Soc.* **2013**, *135*, 3418−3422.
(9) Hsu, W.; Chen, Y. L.; Horng, J. C. *Langmuir* **2012**, *28*, 3194−3199.
(10) (a) Cejas, M. A.; Kinney, W. A.; Chen, C.; Leo, G. C.; Tounge, B. A.; Vinter, J. G.; Joshi, P. P.; Maryanoff, B. E. *J. Am. Chem. Soc.* **2007**, *129*, 2202−2203. (b) Cejas, M. A.; Kinney, W. A.; Chen, C.; Vinter, J. G.; Almond, H. R., Jr; Balss, K. M.; Maryanoff, C. A.; Schmidt, U.; Breslav, M.; Mahan, A.; Lacy, E.; Maryanoff, B. E. *Proc. Natl. Acad. Sci. U.S.A.* **2008**, *105*, 8513−8518.
(11) Kar, K.; Ibrar, S.; Nanda, V.; Getz, T. M.; Kunapuli, S. P.; Brodsky, B. *Biochemistry* **2009**, *48*, 7959−7968.
(12) Chen, C. C.; Hsu, W.; Kao, T. C.; Horng, J. C. *Biochemistry* **2011**, *50*, 2381−2383.
(13) (a) Yamazaki, C. M.; Asada, S.; Kitagawa, K.; Koide, T. *Biopolymers* **2008**, *90*, 816−823. (b) Koide, T.; Homma, D. L.; Asada, S.; Kitagawa, K. *Bioorg. Med. Chem. Lett.* **2005**, *15*, 5230−5233.

(14) Kotch, F. W.; Raines, R. T. *Proc. Natl. Acad. Sci. U.S.A.* **2006**, *103*, 3028−3033.
(15) Rele, S.; Song, Y.; Apkarian, R. P.; Qu, Z.; Conticello, V. P.; Chaikof, E. L. *J. Am. Chem. Soc.* **2007**, *129*, 14780−14787.
(16) (a) Chapman, J. A.; Tzaphlidou, M.; Meek, K. M.; Kadler, K. E. *Electron Microsc. Rev.* **1990**, *3*, 143−182. (b) Kadler, K. E.; Holmes, D. F.; Trotter, J. A.; Chapman, J. A. *Biochem. J.* **1996**, *316*, 1−11.
(17) (a) Gauba, V.; Hartgerink, J. D. *J. Am. Chem. Soc.* **2007**, *129*, 15034−15041. (b) Gauba, V.; Hartgerink, J. D. *J. Am. Chem. Soc.* **2007**, *129*, 2683−2690. (c) Gauba, V.; Hartgerink, J. D. *J. Am. Chem. Soc.* **2008**, *130*, 7509−7515.
(18) O'Leary, L. E.; Fallas, J. A.; Bakota, E. L.; Kang, M. K.; Hartgerink, J. D. *Nat. Chem* **2011**, *3*, 821−828.
(19) (a) Umashankara, M.; Babu, I. R.; Ganesh, K. N. *Chem. Commun.* **2003**, 2606−2607. (b) Babu, I. R.; Ganesh, K. N. *J. Am. Chem. Soc.* **2001**, *123*, 2079−2080.
(20) (a) Hodges, J. A.; Raines, R. T. *J. Am. Chem. Soc.* **2003**, *125*, 9262−9263. (b) DeRider, M. L.; Wilkens, S. J.; Waddell, M. J.; Bretscher, L. E.; Weinhold, F.; Raines, R. T.; Markley, J. L. *J. Am. Chem. Soc.* **2002**, *124*, 2497−2505. (c) Bretscher, L. E.; Jenkins, C. L.; Taylor, K. M.; DeRider, M. L.; Raines, R. T. *J. Am. Chem. Soc.* **2001**, *123*, 777−778. (d) Holmgren, S. K.; Bretscher, L. E.; Taylor, K. M.; Raines, R. T. *Chem. Biol.* **1999**, *6*, 63−70. (e) Holmgren, S. K.; Taylor, K. M.; Bretscher, L. E.; Raines, R. T. *Nature* **1998**, *392*, 666−667.
(21) (a) Okuyama, K.; Hongo, C.; Fukushima, R.; Wu, G.; Narita, H.; Noguchi, K.; Tanaka, Y.; Nishino, N. *Biopolymers* **2004**, *76*, 367−377. (b) Jiravanichanun, N.; Hongo, C.; Wu, G.; Noguchi, K.; Okuyama, K.; Nishino, N.; Silva, T. *ChemBioChem* **2005**, *6*, 1184−1187. (c) Hongo, C.; Noguchi, K.; Okuyama, K.; Tanaka, Y.; Nishino, N. *J. Biochem.* **2005**, *138*, 135−144.
(22) Feng, Y.; Melacini, G.; Taulane, J. P.; Goodman, M. *J. Am. Chem. Soc.* **1996**, *118*, 10351−10358.
(23) (a) Marrington, R.; Seymour, M.; Rodger, A. *Chirality* **2006**, *18*, 680−690. (b) Rodger, A.; Marrington, R.; Geeves, M. A.; Hicks, M.; de Alwis, L.; Halsall, D. J.; Dafforn, T. R. *Phys. Chem. Chem. Phys.* **2006**, *8*, 3161−3171.
(24) Bulheller, B. M.; Rodger, A.; Hicks, M. R.; Dafforn, T. R.; Serpell, L. C.; Marshall, K. E.; Bromley, E. H.; King, P. J.; Channon, K. J.; Woolfson, D. N.; Hirst, J. D. *J. Am. Chem. Soc.* **2009**, *131*, 13305−13314.
(25) (a) Okuyama, K. *Connect. Tissue Res.* **2008**, *49*, 299−310. (b) Okuyama, K.; Xu, X.; Iguchi, M.; Noguchi, K. *Biopolymers* **2006**, *84*, 181−191.
(26) Beaucage, G. J. *Appl. Crystallogr.* **1996**, *29*, 134−146.
(27) Okuyama, K.; Miyama, K.; Mizuno, K.; Bachinger, H. P. *Biopolymers* **2012**, *97*, 607−616.
(28) Kramer, R. Z.; Venugopal, M. G.; Bella, J.; Mayville, P.; Brodsky, B.; Berman, H. M. *J. Mol. Biol.* **2000**, *301*, 1191−1205.
(29) Bella, J.; Eaton, M.; Brodsky, B.; Berman, H. M. *Science* **1994**, *266*, 75−81.
(30) Chanzy, H.; Franc, J. M.; Herbage, D. *Biochem. J.* **1976**, *153*, 139−140.
(31) (a) Hongo, C.; Nagarajan, V.; Noguchi, K.; Kamitori, S.; Okuyama, K.; Tanaka, Y.; Nishino, N. *Polym. J.* **2001**, *33*, 812−818. (b) Okuyama, K.; Hongo, C.; Wu, G.; Mizuno, K.; Noguchi, K.; Ebisuzaki, S.; Tanaka, Y.; Nishino, N.; Bächinger, H. P. *Biopolymers* **2009**, *91*, 361−372. (c) Okuyama, K.; Miyama, K.; Morimoto, T.; Masakiyo, K.; Mizuno, K.; Bächinger, H. P. *Biopolymers* **2011**, *95*, 628−640.
(32) (a) Baxa, U.; Keller, P. W.; Cheng, N.; Wall, J. S.; Steven, A. C. *Mol. Microbiol.* **2011**, *79*, 523−532. (b) Goldsbury, C.; Baxa, U.; Simon, M. N.; Steven, A. C.; Engel, A.; Wall, J. S.; Aebi, U.; Müller, S. A. *J. Struct. Biol.* **2011**, *173*, 1−13. (c) Hodgkinson, J. L.; Horsley, A.; Stabat, D.; Simon, M.; Johnson, S.; da Fonseca, P. C.; Morris, E. P.; Wall, J. S.; Lea, S. M.; Blocker, A. J. *Nat. Struct. Mol. Biol.* **2009**, *16*, 477−485. (d) Sen, A.; Baxa, U.; Simon, M. N.; Wall, J. S.; Sabate, R.; Saupe, S. J.; Steven, A. C. *J. Biol. Chem.* **2007**, *282*, 5545−5550. (e) Baxa, U.; Taylor, K. L.; Wall, J. S.; Simon, M. N.; Cheng, N.; Wickner, R. B.; Steven, A. C. *J. Biol. Chem.* **2003**, *278*, 43717−43727.
(33) Castelletto, V.; Hamley, I. W.; Adamcik, J.; Mezzenga, R.; Gummel, J. *Soft Matter* **2012**, *8*, 217−226.
(34) Yin, P.; Hariadi, R. F.; Sahu, S.; Choi, H. M.; Park, S. H.; Labean, T. H.; Reif, J. H. *Science* **2008**, *321*, 824−826.
(35) Rothemund, P. W. K. *Nature* **2006**, *440*, 297−302.
(36) Lin, C.; Liu, Y.; Rinker, S.; Yan, H. *ChemPhysChem* **2006**, *7*, 1641−1647.
(37) Ke, Y.; Ong, L. L.; Shih, W. M.; Yin, P. *Science* **2012**, *338*, 1177−1183.
(38) Wei, B.; Dai, M.; Yin, P. *Nature* **2012**, *485*, 623−626.
(39) Gradišar, H.; Božič, S.; Doles, T.; Vengust, D.; Hafner-Bratkovič, I.; Mertelj, A.; Webb, B.; Šali, A.; Klavžar, S.; Jerala, R. *Nat. Chem. Biol.* **2013**, *9*, 362−366.
(40) Sleytr, U. B.; Sára, M.; Messner, P.; Pum, D. *J. Cell. Biochem.* **1994**, *56*, 171−176.
(41) Schuster, B.; Sleytr, U. B. *Methods Mol. Biol.* **2013**, *996*, 153−175.
(42) Keith, H. D.; Giannoni, G.; Padden, F. J. *Biopolymers* **1969**, *7*, 775−792.
(43) Xu, F.; Khan, I. J.; McGuinness, K.; Parmar, A. S.; Silva, T.; Murthy, N. S.; Nanda, V. *J. Am. Chem. Soc.* **2013**, *135*, 18762−18765.
(44) Xu, F.; Li, J.; Jain, V.; Tu, R. S.; Huang, Q.; Nanda, V. *J. Am. Chem. Soc.* **2012**, *134*, 47−50.
(45) (a) Pandya, M. J.; Spooner, G. M.; Sunde, M.; Thorpe, J. R.; Rodger, A.; Woolfson, D. N. *Biochemistry* **2000**, *39*, 8728−8734. (b) Ryadnov, M. G.; Woolfson, D. N. *Nat. Mater.* **2003**, *2*, 329−332. (c) Ryadnov, M. G.; Woolfson, D. N. *Angew. Chem., Int. Ed.* **2003**, *42*, 3021−3023. (d) Papapostolou, D.; Smith, A. M.; Atkins, E. D.; Oliver, S. J.; Ryadnov, M. G.; Serpell, L. C.; Woolfson, D. N. *Proc. Natl. Acad. Sci. U.S.A.* **2007**, *104*, 10853−10858. (e) Sharp, T. H.; Bruning, M.; Mantell, J.; Sessions, R. B.; Thomson, A. R.; Zaccai, N. R.; Brady, R. L.; Verkade, P.; Woolfson, D. N. *Proc. Natl. Acad. Sci. U.S.A.* **2012**, *109*, 13266−13271.
(46) (a) Zhang, S.; Holmes, T.; Lockshin, C.; Rich, A. *Proc. Natl. Acad. Sci. U.S.A.* **1993**, *90*, 3334−3338. (b) Marini, D. M.; Hwang, W.; Lauffenburger, D. A.; Zhang, S.; Kamm, R. D. *Nano Lett.* **2002**, *2*, 295−299.
(47) Swanekamp, R. J.; DiMaio, J. T.; Bowerman, C. J.; Nilsson, B. L. *J. Am. Chem. Soc.* **2012**, *134*, 5556−5559.
(48) Marrington, R.; Dafforn, T. R.; Halsall, D. J.; MacDonald, J. I.; Hicks, M.; Rodger, A. *Analyst* **2005**, *130*, 1608−1616.